Title

Shortwave Infrared Fluorofluorophores for Multicolor In Vivo Imaging

Journal

Angewandte Chemie (International ed. in English), 62(6)

ISSN

1521-3773

Authors

Lim, Irene
Lin, Eric Yu
Garcia, Joseph
et al.

Publication Date

2022-12-28

Data Availability

The data associated with this publication are in the supplemental files.

Peer reviewed

Fluorescent Probes Hot Paper

How to cite: *Angew. Chem. Int. Ed.* **2023,** *62,* e202215200
International Edition: doi.org/10.1002/anie.202215200
German Edition: doi.org/10.1002/ange.202215200

Shortwave Infrared Fluorofluorophores for Multicolor *In Vivo* Imaging**

*Irene Lim, Eric Yu Lin, Joseph Garcia, Shang Jia, Robert E. Sommerhalter, Subrata K. Ghosh, John A. Gladysz, and Ellen M. Sletten**

Abstract: Developing chemical tools to detect and influence biological processes is a cornerstone of chemical biology. Here we combine two tools which rely on orthogonality– perfluorocarbons and multiplexed shortwave infrared (SWIR) fluorescence imaging– to visualize nanoemulsions in real time in living mice. Drawing inspiration from fluorous and SWIR fluorophore development, we prepared two SWIR-emissive, fluorous-soluble chromenylium polymethine dyes. These are the most red-shifted fluorous fluorophores– "fluorofluorophores"—to date. After characterizing the dyes, their utility was demonstrated by tracking perfluorocarbon nanoemulsion biodistribution *in vivo.* Using an excitation-multiplexed approach to image two variables simultaneously, we gained insight into the importance of size and surfactant identity on biodistribution.

Introduction

The complexity of living systems has prompted the design of chemical probes and bioorthogonal delivery vehicles which have minimal interactions with the plethora of functionality present in biomolecules. Initially, the concept of bioorthogonality was introduced to describe covalent reactions that can occur in the presence of biomolecules and cells.[1] However, as efforts to bring bioorthogonal chemistries into mammals have increased, its definition has evolved to encompass non-covalent chemistries[2] and nanosystems.[3] One such functionality that falls into the expanded definition of bioorthogonal, that has also seen clinical success, is the perfluorocarbon.[4,5]

Perfluorocarbons (PFCs) are compounds with a large percentage (often >60 wt %) of nonpolarizable sp^3 C–F bonds (Figure 1A), which phase separate from aqueous and organic solutions to form a "fluorous" phase.[6,7] PFCs are not metabolized by mammals and, due to their low boiling points, can be readily cleared by exhalation.[8] In addition, their rigid structure and lack of van der Waals interactions provides a high free volume that leads to impressive gas solubilities.[9] These properties have resulted in a variety of uses of PFCs in mammals including artificial blood,[10] liquid ventilation,[11] enhanced photodynamic therapy,[12] and anti-fouling medical device coatings.[13,14] The unique properties

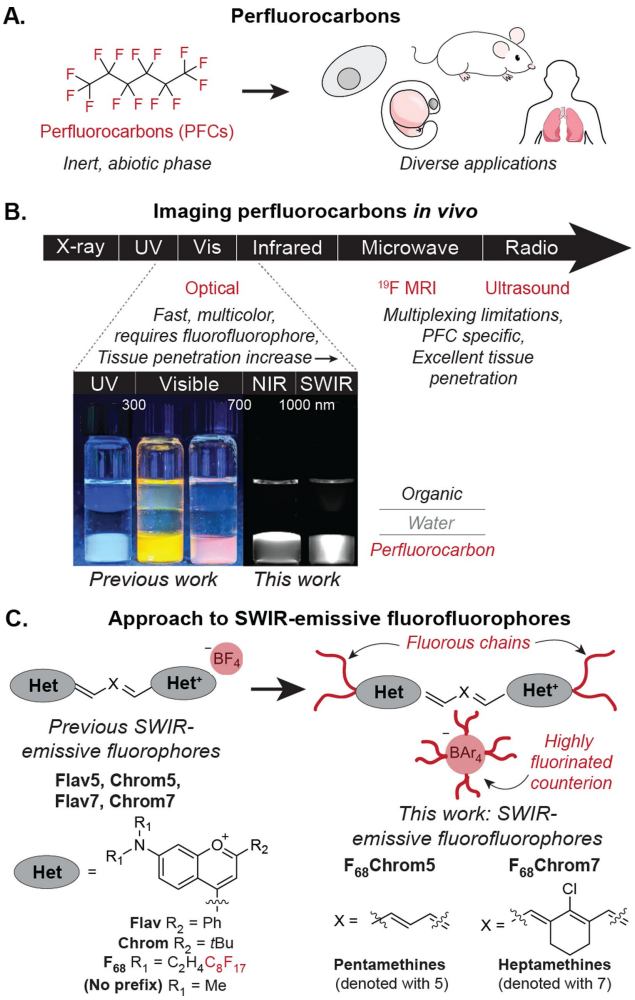

Figure 1. Perfluorocarbons and methods to visualize them. A) Perfluorocarbons and their broad utility. B) *In vivo* imaging methods for perfluorocarbons and their benefits and limitations. C) Transformation of benzopyrylium polymethine dyes into fluorofluorophores.

[*] I. Lim, E. Yu Lin, J. Garcia, S. Jia, E. M. Sletten
Department of Chemistry and Biochemistry, University of California, Los Angeles
607 Charles E. Young Dr. East, Los Angeles, CA 90095 (USA)
E-mail: sletten@chem.ucla.edu

R. E. Sommerhalter, S. K. Ghosh, J. A. Gladysz
Department of Chemistry, Texas A&M University
PO Box 30012, College Station, TX 77842 (USA)

[**] A previous version of this manuscript has been deposited on a preprint server (https://doi.org/10.26434/chemrxiv-2022-vm3jb).

of PFCs have also found use in materials,[15] cells,[16] and model organisms.[17,18]

Tracking PFC materials *in vivo* has traditionally relied on ^{19}F magnetic resonance imaging (MRI), taking advantage of the $^1/_2$ spin of fluorine,[19] or ultrasound imaging, due to the low boiling points of perfluorocarbons (Figure 1B).[20] However, these imaging modalities have limitations in sensitivity, speed, resolution and/or multiplexing.[21,22] An alternative approach to visualizing PFCs is to label them with a "fluorofluorophore," a fluorous-soluble fluorophore.[23] This strategy decouples the identity of the fluorous solvent from the imaging method. Previously, we reported on a palette of fluorofluorophores spanning the visible, far-red, and near infrared (NIR) regions, which have enabled the fluorescent tracking of PFCs in cells and zebrafish (Figure S1).[24] We now extend these fluorophores past 800 nm and report two fluorofluorophores which enable real time imaging of PFCs in mice using shortwave infrared detection on an InGaAs camera. These fluorofluorophores can be used in concert with each other, facilitating direct comparison of two PFC materials in the same animal through a paired imaging approach.[25,26,27] Paired imaging increases the statistical significance of results while halving the overall number of animals required.[28]

The shortwave infrared region of the electromagnetic spectrum (SWIR, 1000–2000 nm) allows for high resolution, non-invasive optical imaging in animals.[29,30] This region is superior to the visible and NIR regions for *in vivo* imaging due to decreased light scattering and minimal background autofluorescence.[31] We previously reported SWIR-emissive flavylium and chromenylium polymethine fluorophores and applied these dyes in an excitation-matched imaging configuration to enable real-time multicolor imaging.[32,33] While displaying excellent brightness for the SWIR region, the flavylium and chromenylium fluorophores are considerably hydrophobic, which brings solubility and aggregation challenges. Here, we combine the strategies of fluorous tagging and counterion exchange (Figure 1C) to produce chromenylium pentamethine and heptamethine dyes with good solubility and brightness in PFC solvents. We use these two fluorophores to simultaneously track different populations of PFC nanoemulsions in mice in the first SWIR paired imaging experiments.

PFC nanoemulsions are droplets of fluorous solvent stabilized by a surfactant. These nanoemulsions were initially developed and FDA-approved for oxygen delivery. They have since been used as a diagnostic as well as for an expanded scope of oxygen delivery applications.[34] Additional efforts harnessing the orthogonal nature of the PFCs for drug or biomolecule delivery are underway by our group and others.[35–37] Our previous work has probed the effect of the surface chemistry of PFC nanoemulsions in cell culture using visible fluorofluorophores.[38] However, we had been unable to perform analogous studies in mice due to the lack of fluorofluorophores available for imaging through tissue. With the development of SWIR fluorofluorophores, we are able to visualize multiple PFC nanoemulsions in animals non-invasively, in real-time, and rapidly assay the biodistribution of these unique soft, bioorthogonal nanomaterials. Indeed, through two-color paired imaging experiments, we demonstrate using minimal mice that varying the size of the PFC nanoemulsions leads to selective accumulation in the spleen within 1 hour, while modification of the surfactant identity results in more subtle biodistribution differences.

Results and Discussion

To generate SWIR-fluorescent, fluorous-soluble dyes, we combined our previous efforts towards fluorofluorophore development with SWIR flavylium and chromenylium fluorophores. We had previously prepared UV and visible fluorofluorophores (Figure S1) from fluorinated aminophenol **1** (Scheme 1). Fortunately, SWIR-emissive **Flav7**, **Chrom7**, and **Chrom5** (Figure 1C) are each prepared in three steps from 3-dimethylaminophenol. Thus, we envisioned **1** to be a suitable building block for fluorous variants of flavylium and chromenylium dyes. We first applied this synthetic pathway to the synthesis of $\mathbf{F_{68}Flav7}$; however, $\mathbf{F_{68}Flav7}$ did not display adequate solubility in fluorous solvents even after exchanging the counterion[39] and we directed our attention to the more soluble chromenylium scaffold.

To prepare fluorous-tagged chromenylium dyes, fluorinated aminophenol **1** underwent Mentzer pyrone synthesis with ethyl pivaloylacetate followed by methyl Grignard

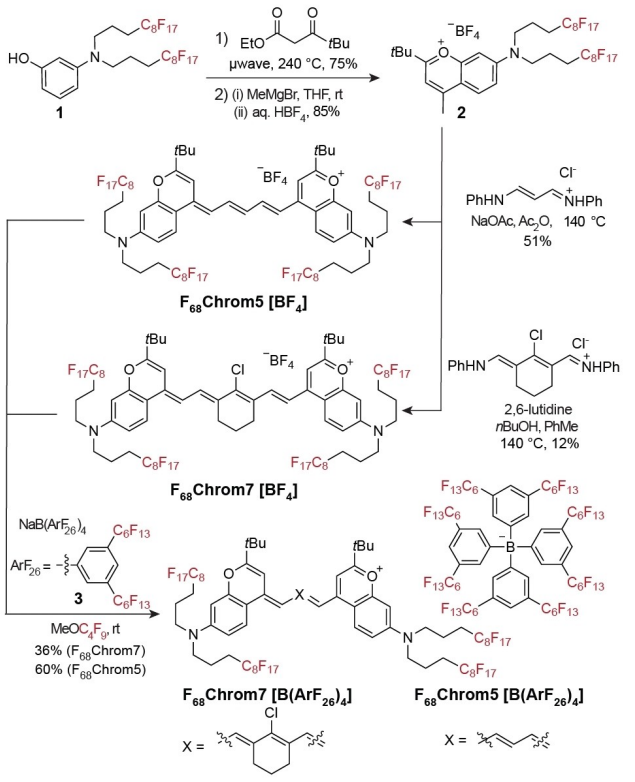

Scheme 1. Synthetic scheme for $\mathbf{F_{68}Chrom5[BF_4]}$ and $\mathbf{F_{68}Chrom7[BF_4]}$. Subsequent counterion exchange with $NaB(ArF_{26})_4$ yields $\mathbf{F_{68}Chrom5[B(ArF_{26})_4]}$ and $\mathbf{F_{68}Chrom7[B(ArF_{26})_4]}$.

addition to yield chromenylium **2** with a BF_4 counteranion. Heterocycle **2** was converted to pentamethine and heptamethine fluorophores by condensation of 0.5 equivalent of *N*-(3-(phenylamino)allylidene) aniline or 1 equivalent of *N*-[(3-(anilinomethylene)-2-chloro-1-cyclohexen-1-yl)methylene]aniline to generate **F_{68}Chrom5[BF_4]** and **F_{68}Chrom7[BF_4]**, respectively. The "F_{68}" corresponds to the number of fluorine atoms on the chromophore scaffold, while the 5 and 7 correspond to the length of the polymethine chain. The counterion is indicated in square brackets. With **F_{68}Chrom5** and **F_{68}Chrom7** in hand, we explored the solubility and photophysical properties of these SWIR-emissive fluorofluorophores.

F_{68}Chrom5[BF_4] and **F_{68}Chrom7[BF_4]** proved to be relatively insoluble in both organic and fluorous solvents, only displaying adequate solubility in solvents known to solubilize semifluorinated compounds such as acetone and hexafluoroisopropanol. These results suggested that more fluorous content was necessary to achieve a true fluorofluorophore. We more than doubled the fluorine content by exchanging the BF_4 counteranion with highly fluorinated aryl borate **3**, denoted here as **$B(ArF_{26})_4$** and previously reported by the Gladysz and Buhlmann groups.[40,41] Gratifyingly, the counterion exchanged dyes **F_{68}Chrom5[$B(ArF_{26})_4$]** and **F_{68}Chrom7[$B(ArF_{26})_4$]** were well-solubilized in PFC solvents such as perfluorooctyl bromide (PFOB) and perfluoromethyl cyclohexane (PFMC). Solubility limit studies were performed in PFOB and PFMC by preparing saturated solutions of the dyes, removing an aliquot, and determining the concentration using absorbance measurements and Beer's law (Figure 2A, Table S2). These studies were especially enlightening for **F_{68}Chrom5**, in which counterion **$B(ArF_{26})_4$** enables ≈7.4-fold higher solubility in perfluoromethylcyclohexane (PFMC) and ≈5.4-fold higher solubility in PFOB. The **$B(ArF_{26})_4$** counterion does not improve solubility limits for **F_{68}Chrom7** as drastically as its pentamethine counterpart.

Another valuable parameter to characterize fluorous solubility is the partition coefficient between PFMC and toluene, deemed $\log_F$.[6] Quantification of the $\log_F$ for the **F_{68}Chrom** dyes also shows a significant change between the **BF_4** and **$B(ArF_{26})_4$** **F_{68}Chrom5** dyes where the preference for toluene is switched to preference for the fluorous solvent in a ≈65-fold increase (Figure 2B). A less drastic, but still significant, change was observed for **F_{68}Chrom7**, displaying a ≈14-fold increase in preference for fluorous solvents upon counterion exchange from **BF_4** to **$B(ArF_{26})_4$**. These data suggest that **F_{68}Chrom5[$B(ArF_{26})_4$]** and **F_{68}Chrom7[$B(ArF_{26})_4$]** are well-retained in PFC even in the presence of hydrophobic species, which is an essential quality for using fluorofluorophores *in vivo*.

We evaluated the photophysical properties of **F_{68}Chrom5[$B(ArF_{26})_4$]** and **F_{68}Chrom7[$B(ArF_{26})_4$]** in PFOB, making comparisons to nonfluorinated variants **Chrom7** and **Chrom5** measured in dichloromethane. The absorbance spectra of both fluorofluorophores are narrow with a small vibronic shoulder indicative of a delocalized cyanine state.[42] The emission is similarly narrow with a long tail, consistent with polymethine fluorophores.[43,44] Note that for

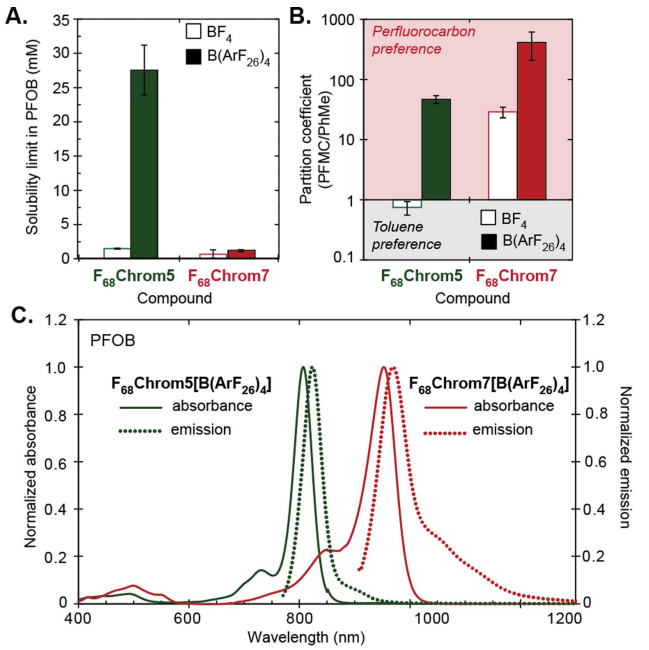

D.

	Chrom5	Chrom7	F_{68}Chrom5 [$B(ArF_{26})_4$]	F_{68}Chrom7 [$B(ArF_{26})_4$]
$\lambda_{max,\ abs}$ (nm)	819	975	807	957
$\lambda_{max,\ em}$ (nm)	836	996	823	969
ε ($M^{-1}cm^{-1}$)	380,000 ± 10,000	252,000 ± 5,000	101,000 ± 5,000	273,000 ± 6,000
Φ_F (%)	28 ± 2	1.70 ± 0.02	47.3 ± 0.4	1.04 ± 0.04
SWIR Brightness	1140	2420	140	1200
	reported in DCM		reported in PFOB	

Figure 2. Photophysical characterizations of **F_{68}Chrom5** and **F_{68}Chrom7**. A) Solubility limit (mM) measured by saturating a perfluorooctylbromide (PFOB) solution. B) Fluorous partition coefficient measured in a perfluoromethylcyclohexane:toluene system at 3 mM. C) Normalized absorption and emission spectra taken in PFOB at 2 μM. D) Table of photophysical properties comparing **F_{68}Chrom** (reported in PFOB) dyes with their organic congeners (reported in dichloromethane). See Table S1 for errors.

F_{68}Chrom5[$B(ArF_{26})_4$] the tail extends above 1000 nm, facilitating imaging with a InGaAs camera. Both fluorous variants displayed a slight blue-shift in λ_{max} from the parent fluorophores, with $\lambda_{max,abs}$ = 957 nm for **F_{68}Chrom7[$B(ArF_{26})_4$]** and $\lambda_{max,abs}$ = 807 nm for **F_{68}Chrom5[$B(ArF_{26})_4$]** (Figure 2C). The absorption coefficients (ε) for **F_{68}Chrom7[$B(ArF_{26})_4$]** and **F_{68}Chrom5[$B(ArF_{26})_4$]** were lower than observed for **Chrom7** and **Chrom5** (Figure 2D), consistent with the effects of PFC solvent on ε observed for other fluorofluorophores.[24] The quantum yield (Φ_F) values for the fluorofluorophores did display deviation from the hydrophobic congeners; however, these values remained good to excellent for their respective regions of the electromagnetic spectrum. The Φ_F = 1.04 % for **F_{68}Chrom7[$B(ArF_{26})_4$]** was lower than that of **Chrom7** (Φ_F = 1.7 %) while the Φ_F of **F_{68}Chrom5[$B(ArF_{26})_4$]** at 47.3 % was significantly higher than the Φ_F of **Chrom5** (Φ_F = 28 %). The most important metric for imaging experiments is the brightness, where overall brightness = $\varepsilon_{max}\Phi_F$ and, relevant to our excitation-based multiplexing experiments, SWIR brightness = $\varepsilon_{max}\alpha\Phi_F$, where α = the percentage of emission above 1000 nm. When

considering overall brightness, the **F_{68}Chrom5[B(ArF_{26})$_4$]** is the superior dye; however, for SWIR imaging experiments the more red-shifted, yet less emissive, **F_{68}Chrom7[B(ArF_{26})$_4$]** displays superior SWIR brightness. Importantly, both fluorofluorophores have sufficient brightness and photostability (Figure S2) for use in real-time, whole animal, imaging experiments, and display monomeric spectral shapes in fluorous solvent.

With fluorofluorophores applicable for use in mice obtained, we demonstrated their *in vivo* utility by tracking perfluorocarbon nanoemulsions. PFC nanoemulsions have a long history of use *in vivo*, yet only one report images them optically in whole animals (structure of fluorophore not disclosed).[45] For our initial studies, we used **Pluronic F-68** as a surfactant[46] and PFOB for the perfluorocarbon,[47] as these components are both FDA-approved. We were able to prepare NIR and SWIR emissive nanoemulsions by predissolving **F_{68}Chrom5** or **F_{68}Chrom7** in PFOB and emulsifying with PBS containing 2.7 wt % **Pluronic F-68** (Figure 3A, S3). This generated unimodal 200 nm-sized emulsions. Using a continuous partition between an aqueous PFC nanoemulsion solution and 1-octanol, we observed <1 % loss of fluorophore to the 1-octanol for dyes **F_{68}Chrom5[B(ArF_{26})$_4$]** and **F_{68}Chrom7[B(ArF_{26})$_4$]**. Notably, for the pentamethine dye the counterion exchange proved important as 30 % leaching was observed when **F_{68}Chrom5[BF_4]** was incorporated in the nanoemulsions (Figure S4). These data are consistent with the solubility and $\log_F$ data.

We first evaluated how emulsions containing **F_{68}Chrom5 [B(ArF_{26})$_4$]** or **F_{68}Chrom7[B(ArF_{26})$_4$]** behaved in mice by performing single color imaging experiments (Figure 3B,C). All *in vivo* experiments were performed with the **B(ArF_{26})$_4$** counterion and for simplicity the counterion will not be defined during the imaging discussions. We injected 100 µL of emulsions labeled with either **F_{68}Chrom5** or **F_{68}Chrom7** and tracked the movement of the emulsions through the vasculature, heart, and liver almost immediately. Both fluorophores enabled video rate imaging at 100 frames per second (fps). There were no significant changes in biodistribution between 1 and 2 days (Figure 3B, C). After 48 hours, an *ex vivo* analysis was performed in which the heart, lungs, sternum, stomach, kidneys, intestines, liver, and spleen were excised and their fluorescence intensity was quantified (Figure 3D, E and S5). As is typical for nanomaterials, we found significant accumulation in the liver and spleen. Importantly, we confirmed that the identity of the dye does not impact the overall trends in biodistribution, which provided support that the dye was not leaching from the PFC and labelling biomolecules outside of the emulsions.

Next, we confirmed that the PFC nanoemulsions containing **F_{68}Chrom5** and **F_{68}Chrom7** could be orthogonally excited and employed in an excitation multiplexed imaging experiment. Excitation at 785 nm (flux set to 50 mW cm^{-2}) and 974 nm (flux set to 100 mW cm^{-2}) were chosen for **F_{68}Chrom5** and **F_{68}Chrom7** nanoemulsions, respectively. Power densities of irradiation were guided by the International Commission on Non-Ionizing Radiation Protection. Experiments in capillaries to decrease crosstalk between

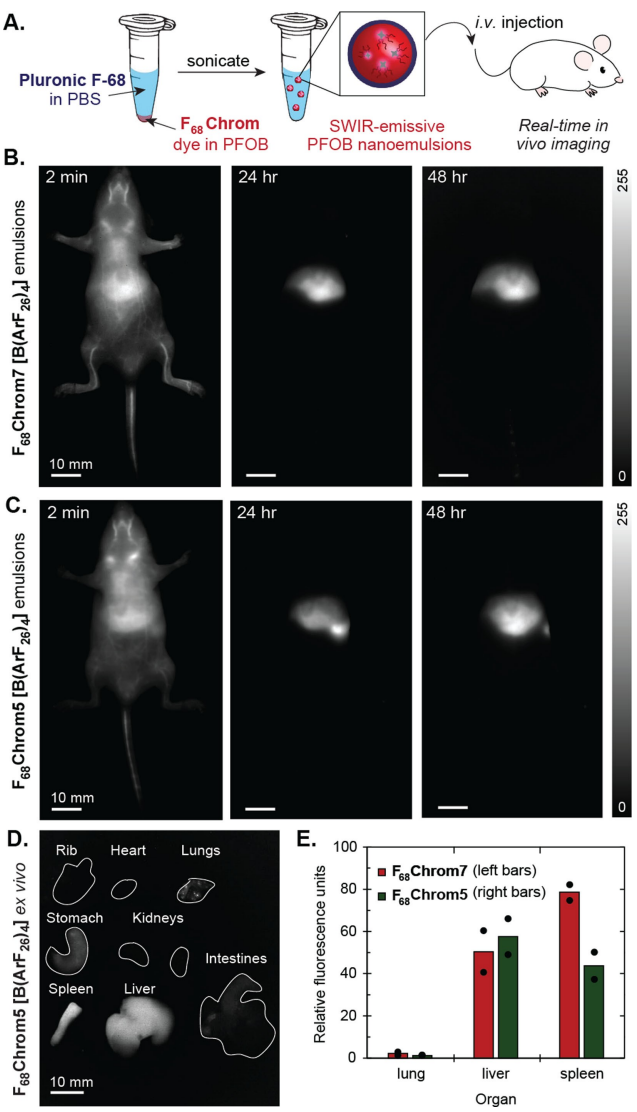

Figure 3. Single color imaging of perfluorocarbon nanoemulsions in nude mice. A) Schematic of PFOB nanoemulsion preparation and subsequent injection *in vivo*. B) Time course of **F_{68}Chrom7**-labelled emulsions (200 nm in diameter) over 48 hours (ex. 974 nm, 100 mW cm^{-2}, 1100 nm LP, 5–10 ms ET). C) Time course of **F_{68}Chrom5**-labelled emulsions (200 nm in diameter) over 48 hours (ex. 785 nm, 50 mW cm^{-2}, 1100 nm LP, 5–7 ms ET). D) *Ex vivo* fluorescence image of **F_{68}Chrom7**. Ex. 974 nm, 100 mW cm^{-2}, 1100 nm LP, 5 ms ET. E) Quantification of *ex vivo* images (see Figure S6 for bar graph with all organs). Signal was normalized to the lowest intensity organ. Dots overlaid on bar graph are individual mice. Red (left bars) indicate PFC nanoemulsions containing **F_{68}Chrom7**, green bars (right bars) indicate PFC nanoemulsions containing **F_{68}Chrom5** (B)–(D). Scale bar = 10 mm.

channels yielded concentrations of 0.012 mM **F_{68}Chrom7** and 0.048 mM **F_{68}Chrom5** as optimal ($\approx$1 % crosstalk, Figure S5).

Spurred by these findings, we looked to vary parameters of the PFC emulsions and compare two different emulsions in the same mouse. These direct two-color comparison experiments are referred to as paired imaging. The first variable we tested was the size of the nanoemulsions. It is

well-established from the use of PFC nanoemulsions for oxygen delivery that the size of the nanoemulsions affects their serum half-lives, with smaller nanoemulsions displaying longer lifetimes in the bloodstream.[48] By varying the amount of **Pluronic F-68** surfactant from 0.6–16 wt %, we were able to prepare nanoemulsions that ranged from 100–300 nm in size (Figure 4A). We loaded the smaller nanoemulsions (100, 150 nm) with **F_{68}Chrom5** and the larger nanoemulsions (200, 300 nm) with **F_{68}Chrom7**. Two paired imaging experiments were performed comparing the 100 and 200 nm emulsions as well as the 150 and 300 nm emulsions. These experiments involved injecting a mix of

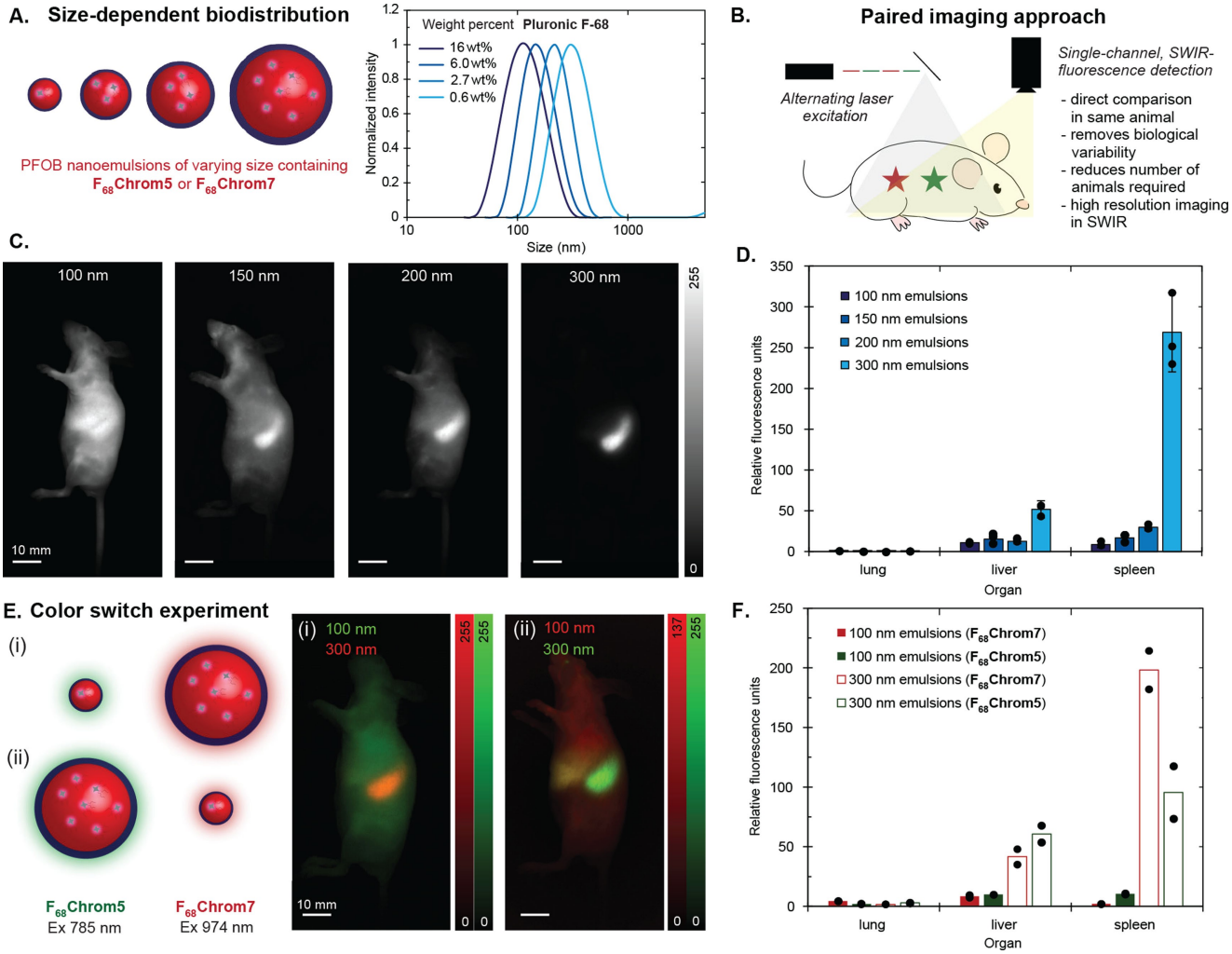

Figure 4. Paired *in vivo* experiments with **Pluronic F-68**–stabilized emulsions. A) Schematic and dynamic light scattering analysis of emulsions. Sizes ranging from 100 to 300 nm were achieved by varying the weight percent of surfactant from 0.6 to 16 wt%. B) Schematic illustrating excitation-multiplexed imaging of an animal labelled with two fluorophores with different absorbance. Triggered orthogonal excitation and subsequent deconvolution allows for color assignment. C) Single color sagittal images of nude mice with varying emulsion sizes, taken at 48 hours post-injection (**F_{68}Chrom7** ex. 974 nm, 100 mW cm^{-2}; **F_{68}Chrom5** ex. 785 nm, 50 mW cm^{-2}; 1100 nm LP, 4–6 ms ET). 100 µL of **F_{68}Chrom5**-labelled 100 nm emulsions and 100 µL of **F_{68}Chrom7**-labelled 200 nm emulsions were *i.v.* injected into one animal. 100 µL of **F_{68}Chrom5**-labelled 150 nm emulsions and **F_{68}Chrom7**-labelled 300 nm emulsions were *i.v.* injected into another animal. See Figure S7 and S8 for replicates. Scale bars = 10 mm. D) *Ex vivo* images were captured after the 48 hour post-injection. The mean fluorescence intensity from each organ was quantified in ImageJ and normalized to the lowest intensity organ value. The quantification of *ex vivo* images is displayed in the bar graph. See Figure S7 and S8 for bar graphs with all organs. Dots overlaid on bar graph are replicates. Error bars are the standard deviation of the mean, where $n = 3$. E) Color switch experiment in which 100 or 300 nm emulsions were labelled with either **F_{68}Chrom5** or **F_{68}Chrom7**. i) Experimental schematic and two color sagittal image of **F_{68}Chrom5**-labelled 100 nm emulsions + **F_{68}Chrom7**-labelled 300 nm emulsions, taken at 48 hours post-injection. 100 µL of each emulsion suspension was injected and imaged with the same acquisition settings as in (C). (ii) Experimental schematic and two color sagittal image of **F_{68}Chrom5**-labelled 300 nm emulsions + **F_{68}Chrom7**-labelled 100 nm emulsions, taken at 48 hours post-injection. 100 µL of each emulsion suspension was injected and imaged with the same acquisition settings as in (C). Scale bars = 10 mm. F) *Ex vivo* images were captured after the 48 hour post-injection images. The mean fluorescence intensity from each organ was quantified in ImageJ, normalized to the lowest intensity organ value, and plotted. See Figure S9 for bar graph with all organs. Dots overlaid on bar graph are replicates. 100 nm emulsions in solid bars; 300 nm emulsion in unfilled bars. Red bars represent **F_{68}Chrom7**. Green bars represent **F_{68}Chrom5**. Red bars are plotted to the right of the green bars.

the PFC nanoemulsions intravenously and immediately imaging with an excitation multiplexed *in vivo* imaging setup (Figure 4B). We observed a striking size-dependent localization with 100 nm emulsions displaying diffuse labeling throughout the animal and the larger nanoemulsions showing liver and spleen localization (Figures 4C, D, S6 and S7). Indeed, the early literature on PFC emulsions corroborates these results, as it has been proposed that the reticuloendothelial macrophages are responsible for depositing perfluorocarbons into the liver and spleen.[49,50] For the case of the 300 nm emulsions, these nanomaterials displayed 5-fold preferential labeling for the spleen vs. the liver, providing a potential delivery vehicle for spleen-targeted immunotherapies.[51] A similar size dependence for spleen localization has been observed for PEG-coated polystyrene (240 nm)[52] and cyanoacrylate nanoparticles (220 nm).[53,54]

To validate the results from the paired imaging studies, we performed a color switch experiment (Figure 4E). We prepared 100 nm emulsions containing **F_{68}Chrom5** and 300 nm emulsions containing **F_{68}Chrom7**. These emulsions were mixed, *i.v.* injected, and the animals were immediately imaged. After 48 hours, the mice were sacrificed and their organs were analyzed *ex vivo*. Simultaneously, we performed an analogous experiment with 100 nm emulsions labeled with **F_{68}Chrom7** and 300 nm emulsions labeled with **F_{68}Chrom5**. We compared the non-invasive imaging results (Figure 4E) as well as *ex vivo* fluorescence quantification (Figure 4F) between the two experiments. We found that overall trends in biodistribution were not impacted by the identity of the dye sequestered in the emulsions (Figures S9, S10).

Finally, we were interested in the effect of the surfactant on the localization of the PFC nanoemulsions. The **Pluronic F-68** surfactant was the original surfactant used for PFC nanoemulsions in humans;[55] yet, it is not readily customized to allow for targeted or smart nanocarriers. We have explored poly(2-oxazoline) (POx)-based amphiphiles as an alternative to **Pluronic F-68** due to their synthetic modularity and control (Figure 5A).[56,57] We have developed amphiphile **4** as a suitable replacement for **Pluronic F-68** and evaluated **4** and its derivatives extensively *in vitro* and *in cellulo*. However, until now, we lacked the fluorofluor-

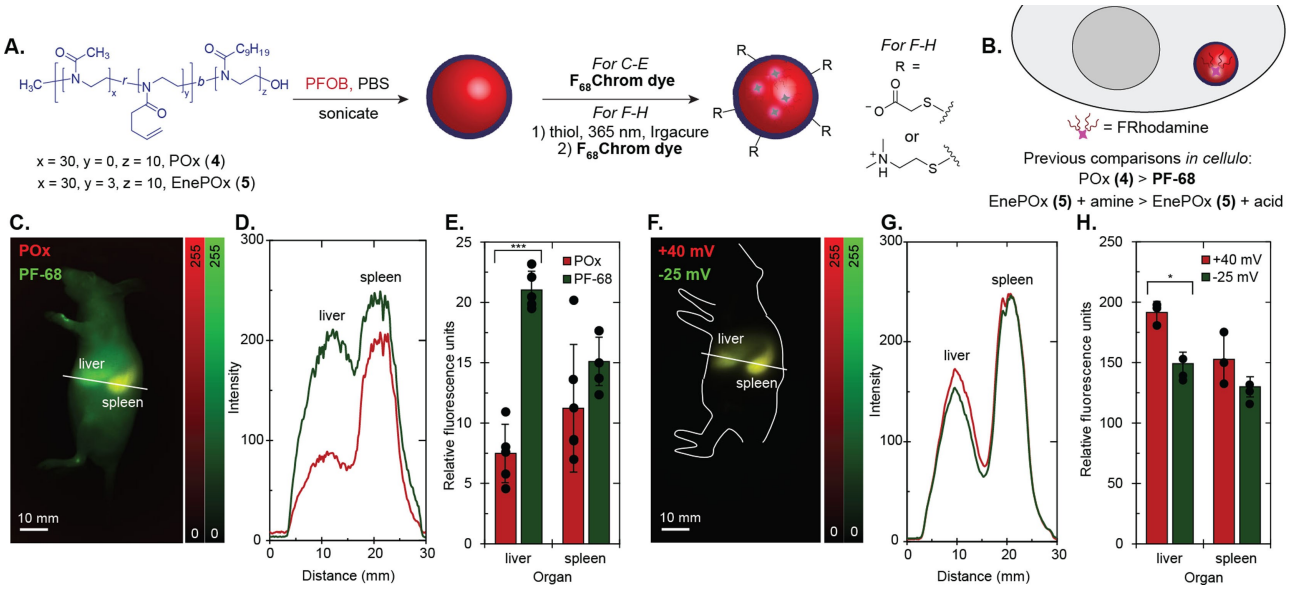

Figure 5. Imaging PFC nanoemulsions stabilized by poly(oxazoline) amphiphiles *in vivo*. A) Schematic of PFOB emulsions stabilized by POx (**4**) or EnePOx (**5**) at 2.7 wt% and subsequent functionalization of emulsions by thiol-ene chemistry. B) Summary of results from previous work *in cellulo* using this methodology. C) Two color sagittal image of an animal injected with **Pluronic F-68** (**PF-68**)-stabilized emulsions and POx-stabilized emulsions, taken at 48 hours post-injection. **F_{68}Chrom7** ex. 974 nm, 100 mW cm^{-2}; **F_{68}Chrom5** ex. 785 nm, 50 mW cm^{-2}; 1100 nm LP, 5–7 ms ET). 100 µL of **F_{68}Chrom5**-labelled PF-68 emulsions and 100 µL of **F_{68}Chrom7**-labelled POx emulsions were *i.v.* injected into one animal. Scale bars = 10 mm. D) Cross-section intensity profile of the line drawn in 5 C, where the green line represents the profile for PF-68 emulsions and the red line represents the profile for POx emulsions. E) *Ex vivo* images were captured after the 48 hour post-injection images. The mean fluorescence intensity from each organ was quantified using ImageJ, normalized to the lowest intensity organ value, and plotted. See Figure S11 for bar graph with all organs. Dots overlaid on bar graph are replicates. Error bars are the standard deviation of the mean, where $n = 5$. Red bars on the left indicate POx emulsions and green bars on the right indicate **Pluronic F-68** emulsions. F) Two color sagittal image of an animal injected with EnePOx-stabilized emulsions, taken at 48 hours post-injection. 100 µL of **F_{68}Chrom5**-labelled negatively charged (−25 mV) emulsions and 100 µL of **F_{68}Chrom7**-labelled positively charged (+40 mV) emulsions were *i.v.* injected into one animal. Images were taken with the same settings as in (C). Scale bars = 10 mm. G) Cross-section intensity profile of the line drawn in (F), where the green line represents the profile for negatively charged emulsions and the red line represents the profile for positively charged emulsions. H) *Ex vivo* images were captured after the 48 hour post-injection images. The mean fluorescence intensity from each organ was quantified using the ImageJ measurement function, normalized to the lowest intensity organ value, and plotted. See Figure S13 for bar graph with all organs. Signal was normalized to the lowest intensity organ. Dots overlaid on bar graph are replicates. Red bars on the left indicate positively charged emulsions and green bars on the right indicate negatively charged emulsions. Error bars are the standard deviation of the mean, where $n = 3$. * = $p < 0.05$, *** = $p < 0.001$.

ophores to properly evaluate POx-stabilized nanoemulsions in mice. With F_{68}**Chrom5** and F_{68}**Chrom7**, we were able to perform direct comparisons of these custom nanoemulsions *in vivo*, focusing on formulations which showed differences *in cellulo* (Figure 5B).

First, we validated that POx-stabilized nanoemulsions were stable *in vivo* and behaved similarly to the previously FDA-approved **Pluronic F-68** nanoemulsions. We compared PFOB-nanoemulsions stabilized by **4** or **Pluronic F-68** containing F_{68}**Chrom5** or F_{68}**Chrom7** in five replicates of a paired imaging experiment (Figures 5C, D and S10). We imaged the mice non-invasively over 48 hours and then performed an *ex vivo* organ analysis. The only significant difference observed was that **4**-stabilized nanoemulsions displayed lower liver uptake than **Pluronic F-68**-stabilized nanoemulsions. Decreased liver uptake is an encouraging result for implementing POx-stabilized nanoemulsions for targeted delivery applications.

The success of the POx-stabilized PFC nanoemulsions *in vivo* sets the stage for advancing these delivery vehicles through defined surface modification. Previously, we had developed a method to decouple the effects of nanoemulsion size and charge *in cellulo* by implementing a post-emulsification modification procedure using thiol-ene chemistry (Figure 5A). This method required alkene-containing amphiphile **5** in place of **4**. Our *in cellulo* work using a rhodamine fluorofluorophore suggested that the surface charge of the nanoemulsions was a significant factor in cellular uptake, particularly for non-macrophage cells.[38]

By using the SWIR-emissive fluorofluorophores, we were able to apply the same methodology used for the cellular microscopy experiments to *in vivo* fluorescence imaging. Briefly, we prepared 250 nm emulsions from **5** and treated half with mercaptoacetic acid and the other half with 2-dimethylaminoethanethiol. The emulsions were irradiated with 365 nm light for 1 hour at 4 °C and purified via centrifugation and resuspension. The acid-functionalized emulsions displayed a zeta potential of −25 mV, and the tertiary amine-functionalized emulsions displayed a zeta potential of +40 mV (Figure S12). These emulsions were then loaded with F_{68}**Chrom5** or F_{68}**Chrom7** and injected into animals. The charged emulsions labelled the liver and spleen predominantly, with an unchanging biodistribution profile from 1 hour after injection to 48 hours (Figure 5F–H). Cross-sections from the paired imaging experiment indicate complete colocalization (Figure 5G, S12). Upon *ex vivo* analysis, we did observe a significant difference ($p = 0.03$) in preference for liver, but the overall change was modest.

Taken together, the new fluorofluorophores F_{68}**Chrom5** and F_{68}**Chrom7** allowed for direct comparisons of PFC nanoemulsions *in vivo.* These experiments demonstrated that POx-stabilized nanoemulsions are promising alternatives for **Pluronic F-68**, displaying lower liver uptake but otherwise similar biodistribution. It appears that the surface charge of the nanoemulsions does not play a large role in mice. This could be due to 1) protein corona effects, which are well-precedented to have a large impact on biodistribution of foreign particles in animals,[58] or 2) the majority of cellular uptake *in vivo* is from macrophages,[59–62] which displayed less charge-dependent uptake in our *in cellulo* studies.[38] Future studies evaluating these hypotheses are underway.

Conclusion

We have prepared two chromenylium fluorofluorophores, F_{68}**Chrom5** and F_{68}**Chrom7**, for imaging in the shortwave infrared region of the electromagnetic spectrum. F_{68}**Chrom5** and F_{68}**Chrom7** were prepared by combining the building block previously employed for the synthesis of visible fluorofluorophores with chromenylium polymethine dye synthesis. Counterion exchange from tetrafluoroborate to the highly fluorinated $B(ArF_{26})_4$ anion enhanced the fluorous solubility, retention, and photophysical properties of the fluorophores. These low energy fluorofluorophores are ideal for imaging through tissue as demonstrated by two-color SWIR imaging in mice with PFC nanoemulsions containing F_{68}**Chrom5** or F_{68}**Chrom7**. Paired experiments allowed for two nanoemulsions to be compared in the same animal, reducing biological variability and animal count. Notable results from the paired PFC nanoemulsion experiments include 1) 300 nm emulsions display significant localization in the spleen over the liver and 2) altering the surfactant from the traditional poly(ethylene glycol) to poly(methyl-2-oxazoline) results in decreased liver accumulation. We expect the F_{68}**Chrom5** and F_{68}**Chrom7** fluorofluorophores will continue to advance our knowledge of PFC nanomaterials *in vivo* as well as be applied to emerging applications of PFCs such as *in vivo* mechanical force measurements[18] and droplet-based sensors.[63]

Acknowledgements

This work was supported by the National Institutes of Health (1R01EB027172 to E.M.S., 5R01GM135380 to E.M.S); Chan Zuckerberg Initiative (2020-225707 to E.M.S.), Tobacco Related Disease Research Program (T32DT4847 to E.Y.L), UCLA (Dissertation Year Fellowship to I.L.; Cota Robles Fellowship to J.G.), and Welch Foundation (A-1656 to J.A.G.) NMR spectrometers are supported by the National Science Foundation under equipment grant no. CHE-1048804. We would also like to thank the Radu group at UCLA Department of Radiology for helpful discussion and members of the Sletten Group for critical reading of the manuscript.

Conflict of Interest

The authors declare no conflict of interest.

Data Availability Statement

The data that support the findings of this study are available in the Supporting Information of this article. Raw and

processed images and videos of all *in vivo* experiments can be found at https://www.ebi.ac.uk/biostudies/studies/S-BIAD554 (Project number S-BIAD554).

Keywords: Biodistribution · Excitation-based Multiplexed Imaging · Fluorescence Imaging · Perfluorocarbon Emulsion · Shortwave Infrared

[1] J. A. Prescher, C. R. Bertozzi, *Nat. Chem. Biol.* **2005**, *1*, 13–21.
[2] N. Yoder, D. Yuksel, L. Dafik, K. Kumar, *Curr. Opin. Chem. Biol.* **2006**, *10*, 576–583.
[3] X. Zhang, Y. Liu, S. Gopalakrishnan, L. Castellanos-Garcia, G. Li, M. Malassiné, I. Uddin, R. Huang, D. C. Luther, R. W. Vachet, V. M. Rotello, *ACS Nano* **2020**, *14*, 4767–4773.
[4] M. A. Miller, E. M. Sletten, *ChemBioChem* **2020**, *21*, 3451–3462.
[5] C. Chirizzi, C. Morasso, A. A. Caldarone, M. Tommasini, F. Corsi, L. Chaabane, R. Vanna, F. B. Bombelli, P. Metrangolo, *J. Am. Chem. Soc.* **2021**, *143*, 12253–12260.
[6] *Handbook of Fluorous Chemistry* (Eds.: J. A. Gladysz, D. P. Curran, I. T. Horváth), Wiley, Hoboken, **2004**.
[7] I. T. Horváth, J. Rábai, *Science* **1994**, *266*, 72–75.
[8] K. C. Lowe, *Comp. Biochem. Physiol. Part A* **1987**, *87*, 825–838.
[9] M. Pierre, J. G. Riess, M. P. Krafft, J. G. Riess, *Adv. Colloid Interface Sci.* **2021**, *184*, 102407.
[10] J. G. Riess, *Artif. Cells Blood Substitutes Biotechnol.* **2005**, *33*, 47–63.
[11] S. Sarkar, A. Paswan, S. Prakas, *Anesth. Essays Res.* **2014**, *8*, 277–282.
[12] Y. Cheng, H. Cheng, C. Jiang, X. Qiu, K. Wang, W. Huan, A. Yuan, J. Wu, Y. Hu, *Nat. Commun.* **2015**, *6*, 8785.
[13] S. Krishnan, C. J. Weinman, C. K. Ober, *J. Mater. Chem.* **2008**, *18*, 3405–3413.
[14] J. Lv, Y. Cheng, *Chem. Soc. Rev.* **2021**, *50*, 5435–5467.
[15] L. D. Zarzar, V. Sresht, E. M. Sletten, J. A. Kalow, D. Blankschtein, T. M. Swager, *Nature* **2015**, *518*, 520–524.
[16] M. L. Fabiilli, J. A. Lee, O. D. Kripfgans, P. L. Carson, J. B. Fowlkes, *Pharm. Res.* **2010**, *27*, 2753–2765.
[17] O. Campàs, T. Mammoto, S. Hasso, R. A. Sperling, D. O'Connell, A. G. Bischof, R. Maas, D. A. Weitz, L. Mahadevan, D. E. Ingber, *Nat. Methods* **2014**, *11*, 183–189.
[18] A. Mongera, P. Rowghanian, H. J. Gustafson, E. Shelton, D. A. Kealhofer, E. K. Carn, F. Serwane, A. A. Lucio, J. Giammona, O. Campàs, *Nature* **2018**, *561*, 401–405.
[19] I. Tirotta, V. Dichiarante, C. Pigliacelli, G. Cavallo, G. Terraneo, F. B. Bombelli, P. Metrangolo, G. Resnati, *Chem. Rev.* **2015**, *115*, 1106–1129.
[20] D. Cosco, E. Fattal, M. Fresta, N. Tsapis, *J. Fluorine Chem.* **2015**, *171*, 18–26.
[21] D. Janasik, T. Krawczyk, *Chem. Eur. J.* **2022**, *28*, e202102556.
[22] G. Pirovano, S. Roberts, S. Kossatz, T. Reiner, *J. Nucl. Med.* **2020**, *61*, 1419–1427.
[23] E. M. Sletten, T. M. Swager, *J. Am. Chem. Soc.* **2014**, *136*, 13574–13577.
[24] I. Lim, A. Vian, H. L. van de Wouw, R. A. Day, C. Gomez, Y. Liu, A. L. Rheingold, O. Campàs, E. M. Sletten, *J. Am. Chem. Soc.* **2020**, *142*, 16072–16081.
[25] D. Pressman, E. D. Day, M. Blau, *Cancer Res.* **1957**, *17*, 845–50.
[26] K. M. Tichauer, K. S. Samkoe, K. J. Sexton, S. K. Hextrum, H. H. Yang, W. S. Klubben, J. R. Gunn, T. Hasan, B. W. Pogue, *Mol. Imaging Biol.* **2012**, *14*, 584–592.
[27] C. Li, X. Xu, N. McMahon, O. Alhaj Ibrahim, H. A. Sattar, K. M. Tichauer, *Contrast Media Mol. Imaging* **2019**, *2019*, 7561862.
[28] C. L. Schreiber, C. Zhai, J. M. Dempsey, H. H. McGarraugh, B. P. Matthews, C. R. Christmann, B. D. Smith, *Bioconjugate Chem.* **2020**, *31*, 214–223.
[29] G. Hong, A. L. Antaris, H. Dai, *Nat. Biomed. Eng.* **2017**, *1*, 10.
[30] Kenry, Y. Duan, B. Liu, *Adv. Mater.* **2018**, *30*, 1802394.
[31] F. Ding, Y. Zhan, X. Lu, Y. Sun, *Chem. Sci.* **2018**, *9*, 4370–4380.
[32] E. D. Cosco, A. L. Spearman, S. Ramakrishnan, J. G. P. Lingg, M. Saccomano, M. Pengshung, B. A. Arús, K. C. Y. Wong, S. Glasl, V. Ntziachristos, M. Warmer, R. R. McLaughlin, O. T. Bruns, E. M. Sletten, *Nat. Chem.* **2020**, *12*, 1123–1130.
[33] E. D. Cosco, B. A. Arús, A. L. Spearman, T. L. Atallah, I. Lim, O. S. Leland, J. R. Caram, T. S. Bischof, O. T. Bruns, E. M. Sletten, *J. Am. Chem. Soc.* **2021**, *143*, 6836–6846.
[34] C. Zhang, K. Yan, C. Fu, H. Peng, C. J. Hawker, A. K. Whittaker, *Chem. Rev.* **2022**, *122*, 167–208.
[35] J. N. Sloand, T. T. Nguyen, S. A. Zinck, E. C. Cook, T. J. Zimudzi, S. A. Showalter, A. B. Glick, J. C. Simon, S. H. Medina, *ACS Nano* **2020**, *14*, 4061–4073.
[36] M. Herneisey, P. F. Salcedo, T. Domenech, C. Bagia, S. S. George, R. Tunney, S. Velankar, T. K. Hitchens, J. M. Janjic, *ACS Med. Chem. Lett.* **2020**, *11*, 2032–2040.
[37] J. M. Nichols, C. V. Crelli, L. Liu, H. V. Pham, J. M. Janjic, A. J. Shepherd, *J. Neuroinflammation* **2021**, *18*, 299.
[38] D. A. Estabrook, A. F. Ennis, R. A. Day, E. M. Sletten, *Chem. Sci.* **2019**, *10*, 3994–4003.
[39] E. D. Cosco, Polymethine Fluorophores for *In Vivo* Shortwave Infrared Imaging, University of California, Los Angeles, **2020**.
[40] S. K. Ghosh, A. S. Ojeda, J. Guerrero-Leal, N. Bhuvanesh, J. A. Gladysz, *Inorg. Chem.* **2013**, *52*, 9369–9378.
[41] P. G. Boswell, P. Bühlmann, *J. Am. Chem. Soc.* **2005**, *127*, 8958–8959.
[42] S. Pascal, A. Haefele, C. Monnereau, A. Charaf-Eddin, D. Jacquemin, B. Le Guennic, C. Andraud, O. Maury, *J. Phys. Chem. A* **2014**, *118*, 4038–4047.
[43] S. Zhu, R. Tian, A. L. Antaris, X. Chen, H. Dai, *Adv. Mater.* **2019**, *31*, 1900321.
[44] S. Zhu, B. C. Yung, S. Chandra, G. Niu, A. L. Antaris, X. Chen, *Theranostics* **2018**, *8*, 4141–4151.
[45] A. Balducci, Y. Wen, Y. Zhang, B. M. Helfer, T. K. Hitchens, W. S. Meng, A. K. Wesa, J. M. Janjic, *Oncoimmunology* **2013**, *2*, e23034.
[46] A. Pitto-Barry, N. P. E. Barry, *Polym. Chem.* **2014**, *5*, 3291–3297.
[47] P. E. Keipert, *Artif. Cells Blood Substitutes Biotechnol.* **1995**, *23*, 381–394.
[48] J. G. Riess, M. Le Blanc, *Pure Appl. Chem.* **1982**, *54*, 2383–2406.
[49] Y. Tsuda, K. Yamanouchi, K. Yokoyama, T. Suyama, M. Watanabe, H. Ohyanagi, Y. Saitoh, *Biomater. Artif. Cells Artif. Organs* **1988**, *16*, 473–483.
[50] S. F. Flaim, *Artif. Cells Blood Substitutes Biotechnol.* **1994**, *22*, 1043–1054.
[51] Y. Zhai, X. He, Y. Li, R. Han, Y. Ma, P. Gao, Z. Qian, Y. Gu, S. Li, *Sci. Adv.* **2021**, *7*, eabi6326.
[52] S. M. Moghimi, H. Hedeman, I. S. Muir, L. Illum, S. S. Davis, *Biochim. Biophys. Acta Gen. Subj.* **1993**, *1157*, 233–240.
[53] C. Fang, B. Shi, Y.-Y. Pei, M.-H. Hong, J. Wu, H.-Z. Chen, *Eur. J. Pharm. Sci.* **2006**, *27*, 27–36.
[54] J.-W. Yoo, E. Chambers, S. Mitragotri, *Curr. Pharm. Des.* **2010**, *16*, 2298–2307.
[55] T. Mitsuno, H. Ohyanagi, R. Naito, *Ann. Surg.* **1982**, *195*, 60–69.

[56] R. Hoogenboom, *Angew. Chem. Int. Ed.* **2009**, *48*, 7978–7994; *Angew. Chem.* **2009**, *121*, 8122–8138.
[57] R. A. Day, D. A. Estabrook, C. Wu, J. O. Chapman, A. J. Togle, E. M. Sletten, *ACS Appl. Mater. Interfaces* **2020**, *12*, 38887–38898.
[58] R. Cai, C. Chen, *Adv. Mater.* **2019**, *31*, 1805740.
[59] L. Wu, F. Liu, S. Liu, X. Xu, Z. Liu, X. Sun, *Int. J. Nanomed.* **2020**, *15*, 7377–7395.
[60] J. Jägers, A. Wrobeln, K. B. Ferenz, *Pflugers Arch. Eur. J. Physiol.* **2021**, *473*, 139–150.
[61] R. Holman, O. Lorton, P. C. Guillemin, S. Desgranges, C. Contino-Pépin, R. Salomir, *Front. Chem.* **2022**, *9*, 810029.
[62] A. H. Schmieder, S. D. Caruthers, J. Keupp, S. A. Wickline, G. M. Lanza, *Engineering* **2015**, *1*, 475–489.
[63] J. M. Joseph, M. R. Gigliobianco, B. M. Firouzabadi, R. Censi, P. Di Martino, *Pharmaceutica* **2022**, *14*, 382.

Manuscript received: October 16, 2022
Accepted manuscript online: December 5, 2022
Version of record online: December 28, 2022